

Optimizing the Pd Sites in Pure Metallic Aerogels for Efficient Electrocatalytic H₂O₂ Production

Xin Zhang, Cui Wang, Kai Chen, Adam H. Clark, René Hübner, Jinhua Zhan, Liang Zhang,* Alexander Eychmüller,* and Bin Cai*

Decentralized electrochemical production of hydrogen peroxide (H₂O₂) is an attractive alternative to the industrial anthraquinone process, the application of which is hindered by the lack of high-performance electrocatalysts in acidic media. Herein, a novel catalyst design strategy is reported to optimize the Pd sites in pure metallic aerogels by tuning their geometric environments and electronic structures. By increasing the Hg content in the Pd–Hg aerogels, the Pd–Pd coordination is gradually diminished, resulting in isolated, single-atom-like Pd motifs in the Pd₂Hg₅ aerogel. Further heterometal doping leads to a series of M–Pd₂Hg₅ aerogels with an unalterable geometric environment, allowing for sole investigation of the electronic effects. Combining theoretical and experimental analyses, a volcano relationship is obtained for the M–Pd₂Hg₅ aerogels, demonstrating an effective tunability of the electronic structure of the Pd active sites. The optimized Au–Pd₂Hg₅ aerogel exhibits an outstanding H₂O₂ selectivity of 92.8% as well as transferred electron numbers of ≈ 2.1 in the potential range of 0.0–0.4 V_{RHE}. This work opens a door for designing metallic aerogel electrocatalysts for H₂O₂ production and highlights the importance of electronic effects in tuning electrocatalytic performances.

via the oxygen reduction reaction (ORR), which can be operated at ambient conditions using renewable energy resources with minimal capital investments.^[3] This strategy has been extensively investigated to achieve promising efficiencies by designing novel electrocatalysts based on nanocarbons,^[4] transition metals,^[5] and noble metals.^[6] It is worth mentioning that, owing to the low stability of H₂O₂ in basic conditions and the lack of efficient anion-exchange membranes, the production of H₂O₂ in acidic media is more suitable for practical applications, yet challenging.^[7]

Platinum group metals hold promise in the acidic production of H₂O₂ owing to their excellent ORR activity and adequate stability under harsh conditions compared with the 3d transition metal-based catalysts.^[8] Unfortunately, the ORR on noble-metal-based surfaces tends to proceed through the four-electron (4e) pathway to

produce H₂O, rather than the two-electron (2e) pathway to produce H₂O₂.^[9] Thus, improving the selectivity of noble metals is of significant importance while maximizing their electrocatalytic activity. In principle, the effective strategy to increase the selectivity is to suppress the O–O bond cleavage, which has been proven by isolating the metal sites to maintain the end-on-type adsorption (rather than μ -peroxo coordination) of O₂ molecules.^[10] For instance, single-atom Pd or Pt supported on carbons,^[11] sulfides,^[12] and nitrides^[6d] has demonstrated improved

1. Introduction

Hydrogen peroxide (H₂O₂), as a valuable and environmentally friendly oxidizing agent, plays an indispensable role in the fields of chemical synthesis, renewable energy, and wastewater treatment.^[1] The current industrial production of H₂O₂ via the anthraquinone process suffers from inherent complexity, high energy consumption, high production cost, and environmental pollution.^[2] An appealing alternative is the electrochemical approach

X. Zhang, J. Zhan, B. Cai
School of Chemistry and Chemical Engineering
Shandong University
Jinan 250100, China
E-mail: bin.cai@sdu.edu.cn

C. Wang, A. Eychmüller
Physical Chemistry
Technische Universität Dresden
01069 Dresden, Germany
E-mail: alexander.eychmueller@chemie.tu-dresden.de

 The ORCID identification number(s) for the author(s) of this article can be found under <https://doi.org/10.1002/adma.202211512>.

© 2023 The Authors. Advanced Materials published by Wiley-VCH GmbH. This is an open access article under the terms of the Creative Commons Attribution License, which permits use, distribution and reproduction in any medium, provided the original work is properly cited.

K. Chen, L. Zhang
Center for Combustion Energy
School of Vehicle and Mobility
State Key Laboratory of Automotive Safety and Energy
Tsinghua University
Beijing 100084, China
E-mail: zhangbright@tsinghua.edu.cn

A. H. Clark
Laboratory for Synchrotron Radiation and Femtochemistry
Paul Scherrer Institute
Villigen 5232, Switzerland

R. Hübner
Helmholtz-Zentrum Dresden-Rossendorf
Institute of Ion Beam Physics and Materials Research
Bautzner Landstrasse 400, 01328 Dresden, Germany

DOI: 10.1002/adma.202211512

selectivity for the two-electron pathway. Dilution by alloying with catalytically inert Hg,^[6b] Au,^[13] or Se^[6c] also leads to a single-atom-like coordination feature of the Pd or Pt sites, thus facilitating the selective production of H₂O₂. However, the nonuniform structure in these catalysts hinders the identification of active sites, the mechanistic study of electronic and geometric effects, as well as further rational optimization. Meanwhile, the tedious fabrication process and the inevitable corrosion issue of carbon support add extra obstacles toward practical application.

In this work, we address the abovementioned challenges by developing a systematic strategy to optimize the Pd active sites in pure metallic aerogels. Benefiting from the self-supportability, high porosity, and interconnected network structures, metallic aerogels have demonstrated significant potential as next-generation electrocatalysts, yet are barely being explored in H₂O₂ production.^[14] The optimization strategy starts with the construction of Hg-coordinated, single-atom-like Pd motifs with diminished Pd–Pd coordination, followed by the fine tuning of the electronic structure by doping different heterometals. By optimizing the Hg content, improved selectivity, activity, and stability have been achieved upon the intermetallic Pd₂Hg₅ aerogel. The preservation of the geometric environment upon further heterometal doping was demonstrated by various structural charac-

terizations, such as X-ray diffraction (XRD) and X-ray absorption spectroscopy (XAS), resulting in the controlled modulation of the electronic effects.^[15] Combining density functional theory (DFT) and electrochemistry studies, we reveal the role of ligand effects in manipulating the activity and selectivity of Pd sites and report a structure–property relationship of the M–Pd₂Hg₅ aerogels. As a result, the as-obtained Au–Pd₂Hg₅ aerogel exhibits a high H₂O₂ selectivity of 92.8% in the potential range of 0.0–0.4 V_{RHE}, which could be sustained for 10 h without decay. Our work, to the best of our knowledge, provides the first strategy to modulate the single-atom site in a pure metallic substrate and holds promise for the rational design of novel catalysts in the future.

2. Results and Discussion

2.1. Design and Characterization of the Pd–Hg Aerogels

Figure 1a illustrates the design concept of diminishing the Pd–Pd coordination by tuning Pd–Hg alloys, which reveals the atomic coordination of the Pd site of pure Pd, PdHg, and Pd₂Hg₅ alloys. Apparently, the Pd–Pd coordination is progressively replaced by Pd–Hg (or Hg–Pd) with increasing the Hg content,

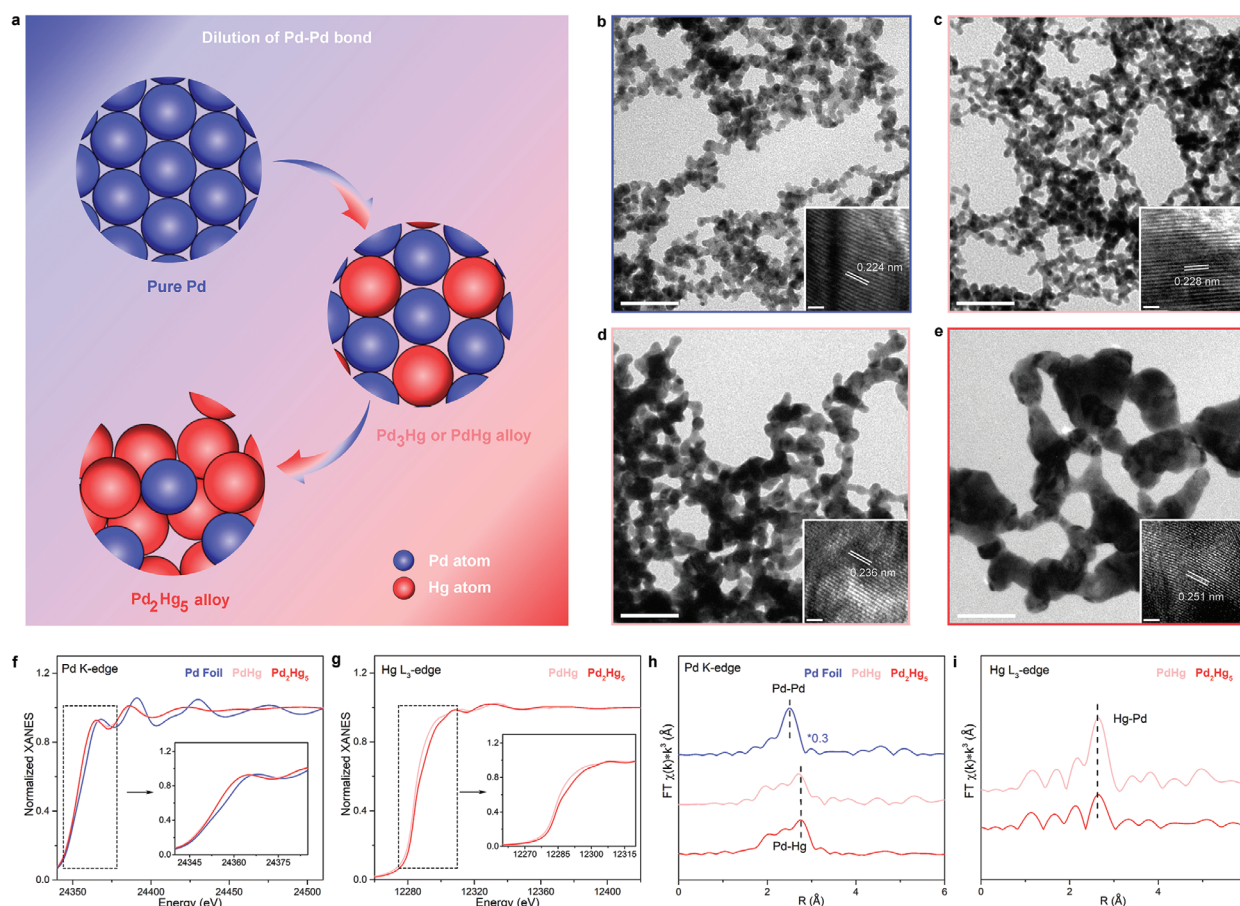


Figure 1. Design and characterization of the Pd–Hg aerogels. a) Schematic of the design concept of diminishing the Pd–Pd coordination in the Pd–Hg aerogels by increasing Hg content. b–d) TEM images of the pure Pd (b), Pd₃Hg (c), PdHg (d), and Pd₂Hg₅ (e) aerogels. The insets display the high-resolution TEM (HR-TEM) images. The scale bars in the TEM and HR-TEM images are 50 and 1 nm, respectively. f,g) The normalized Pd K-edge (f) and Hg L₃-edge (g) XANES spectra, as well as h,i) the Fourier transforms of the *k*²-weighted Pd K-edge (h) and *k*²-weighted Hg L₃-edge (i) radial distance space spectra of the Pd–Hg aerogels. The insets of f,g) are the local enlargements.

which reduces the possibility of μ -peroxo coordinated adsorption of O_2 molecules and prompts the 2e pathway.^[6b] In light of this principle, for the first time, a series of Pd–Hg aerogels was fabricated via a facile one-step gelation method.^[16] The as-prepared Pd–Hg aerogels show highly porous nanostructures (Figure S1, Supporting Information). Interestingly, the incorporation of Hg into the aerogel system leads to accelerated gelation kinetics, as well as a variation of the ligament size of the Pd–Hg aerogels (Figure S2, Supporting Information). As depicted in Figure 1b–d, the average ligament size increases from 12 nm (pure Pd aerogel) to 25 nm (Pd₂Hg₅ aerogel), indicating a diminishing of specific surface areas (Figure S2c, Supporting Information). Meanwhile, a lattice expansion with increasing Hg content has also been observed (shown in the insets of Figure 1b–e), which can be ascribed to the low cohesive energy and larger atomic size of Hg.^[17] This phenomenon is consistent with the XRD analysis, which demonstrates shifts of the characteristic peaks toward smaller angles with increasing Hg content (Figure S2d, Supporting Information). It is worth mentioning that the Pd₂Hg₅ phase is the highest Hg content that could be achieved in our Pd–Hg aerogels. Further increasing the Hg content leads to the formation of separated phases (i.e., Hg oxides; see Figure S2f in the Supporting Information).

The geometric and electronic structures of the Pd–Hg aerogels have been further investigated by both X-ray absorption near-edge spectroscopy (XANES) and extended X-ray absorption fine structure (EXAFS). As shown in the Pd K-edge XANES analysis (Figure 1f), the PdHg and Pd₂Hg₅ aerogels show an almost identical absorption edge energy in the range of 24 344–24 575 eV, as well as similar white line intensities, which are both slightly lower than that of a Pd foil. This implies that the Hg-alloying promotes the maintenance of the reduced state of Pd under ambient

conditions. Due to the lack of a Hg reference, such analysis for the Hg L₃-edge could only be performed within the Pd–Hg aerogels. As shown in Figure 1g, the Hg L₃-edge XANES of the Pd₂Hg₅ aerogel shifts to higher energy compared to that of the PdHg aerogel, indicative of a more oxidized state of the Hg content in the Pd₂Hg₅ aerogel. This phenomenon agrees with the Hg alloying, which implies a possible charge transfer from Hg to Pd due to a higher Fermi level of Hg. As shown in Figure 1h, the radial distance space spectra $\chi(R)$ for the Pd K-edge of the Pd–Hg aerogels show distinct peaks at about 2.7 Å, which are ascribed to the scattering path of the Pd–Hg bond. Meanwhile, the scattering path of the Pd–Pd bond, revealed by the peaks at about 2.5 Å in the Pd foil, could hardly be observed in the Pd–Hg aerogels, indicating a dramatic suppression of Pd–Pd coordination. The radial distance space spectra $\chi(R)$ for the Hg L₃-edge of the Pd–Hg aerogels (Figure 1i) show well-defined peaks of the scattering path of the Hg–Pd bond at around 2.7 Å, which is consistent with the $\chi(R)$ for the Pd K-edge.

2.2. Electrocatalytic Performance of the Pd–Hg Aerogels

The modulation of the Pd sites in terms of geometric structure in the Pd–Hg aerogels has been investigated by cyclic voltammetry (CV) in N_2 -saturated 0.1 M HClO₄ electrolyte. The potential range of 0.09–0.30 V_{RHE} has widely been employed to study the underpotential deposition (UPD) of hydrogen, while the range of 0.62–0.90 V_{RHE} suits the surface Pd oxidation and reduction.^[18] The pure Pd aerogel shows well-defined redox peaks in the hydrogen range and the surface Pd oxidation (Figure 2a). Upon increasing the Hg content (i.e., the Pd–Hg aerogels), these redox peaks are remarkably decreased and ultimately become negligible

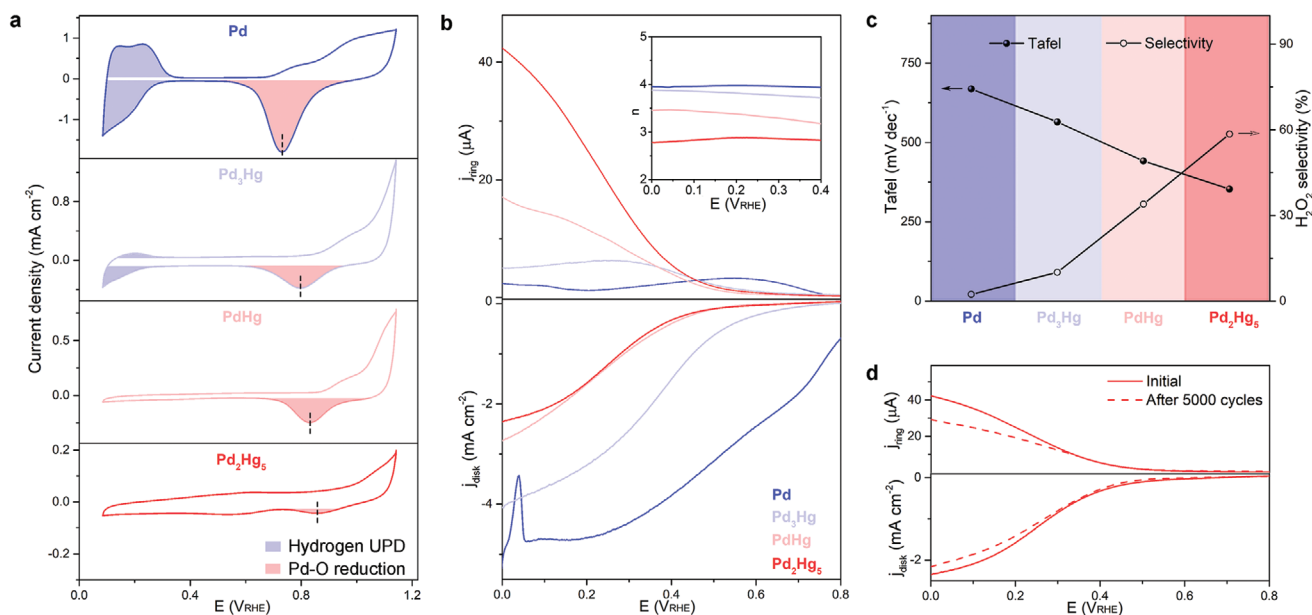


Figure 2. Electrocatalytic performance of the Pd–Hg aerogels. a) Cyclic voltammetry (CV) curves of the pure Pd and Pd–Hg aerogels in 0.1 M N_2 -saturated HClO₄ with a scan rate of 50 mV s⁻¹. UPD represents underpotential deposition. b) Linear sweep voltammetry (LSV) curves of the pure Pd and Pd–Hg aerogels in 0.1 M O_2 -saturated HClO₄ at a rotation rate of 1600 rpm and a scan rate of 20 mV s⁻¹, as well as the detected H_2O_2 currents on the Pt ring electrode at a fixed potential of 1.2 V_{RHE}. The inset shows the calculated transferred electron number. c) The corresponding ORR Tafel slope and the H_2O_2 selectivity (at 0.2 V_{RHE}) of the pure Pd and Pd–Hg aerogels. d) LSV curves of the Pd₂Hg₅ aerogel before and after continuous CV cycling within the potential range of 0.1–0.67 V_{RHE} in O_2 -saturated HClO₄ with a scan rate of 100 mV s⁻¹.

for the Pd_2Hg_5 aerogel (Figure S3, Supporting Information), which is ascribed to the surface enrichment of Hg.^[6a,b] The complete disappearance of hydrogen UPD peaks for the Pd_2Hg_5 aerogel demonstrates the successful construction of single-atom-like Pd sites, as the hydrogen adsorption requires at least Pd–Pd dimers.^[19] Moreover, the reduction peak of surface Pd–O shifts to more positive potentials with increasing Hg contents, indicative of a weaker adsorption of hydroxyl intermediates.

The electrocatalytic performance of the Pd–Hg aerogels has been evaluated using a rotating ring–disk electrode in O_2 -saturated 0.1 M HClO_4 electrolyte with the collection efficiency of about 20% (Figure S4, Supporting Information). The pure Pd aerogel shows an electron transfer number of $3.98 e^-$, which is consistent with the typical 4e pathway (Figure 2b). With the increasing Hg content in the Pd–Hg aerogels, the ring current prominently increases and reaches a maximum of $25.9 \mu\text{A}$ at $0.2 V_{\text{RHE}}$ for the

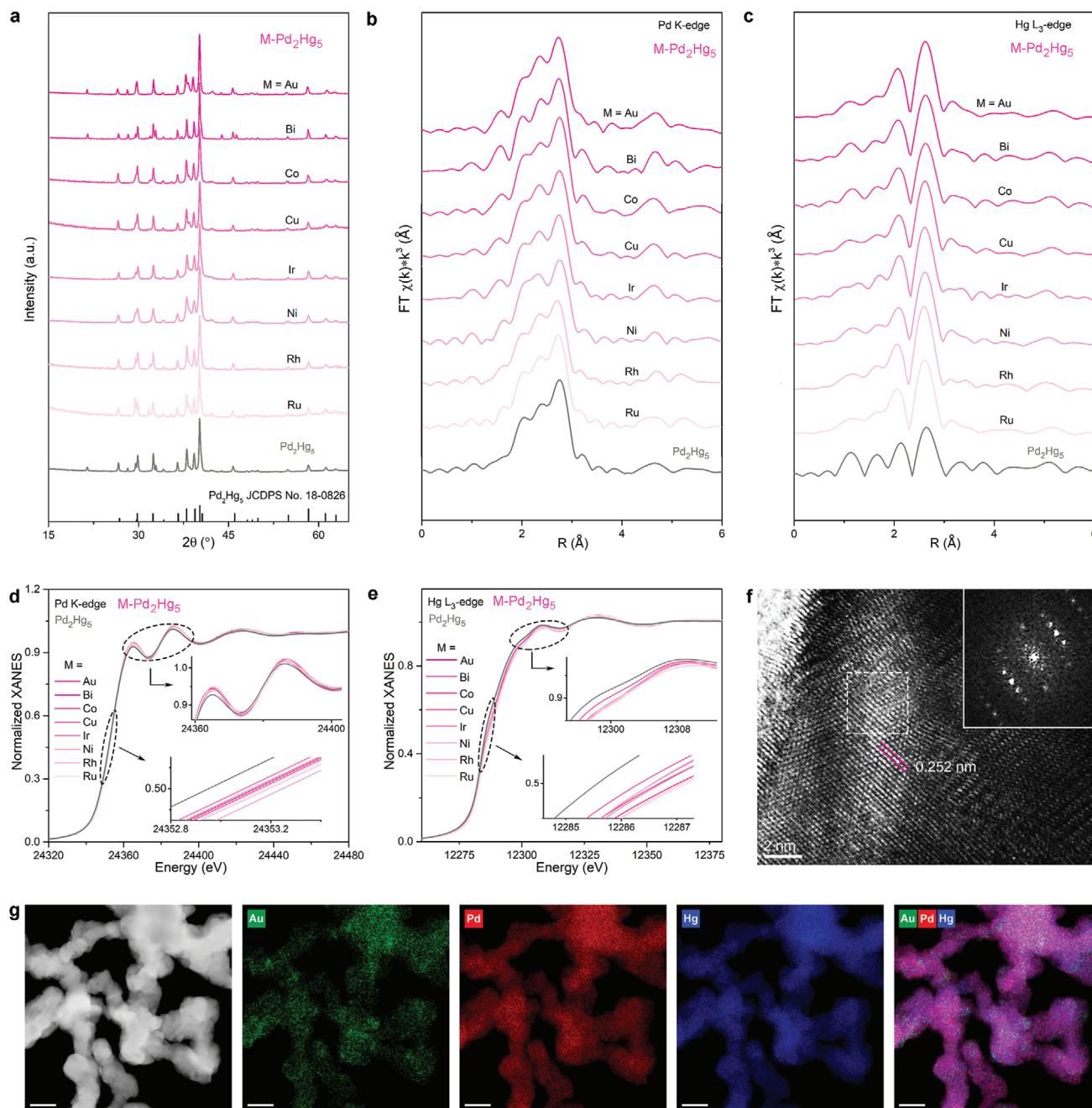


Figure 3. Characterization of the heterometal-doped $\text{M-Pd}_2\text{Hg}_5$ aerogels. a) XRD patterns, and b,c) the Fourier transform k^2 -weighted Pd K-edge (b) and k^2 -weighted Hg $\text{L}_{3\text{-edge}}$ (c) radial distance space spectra of the $\text{M-Pd}_2\text{Hg}_5$ aerogels. d,e) Normalized Pd K-edge (d) and Hg $\text{L}_{3\text{-edge}}$ (e) XANES spectra of the $\text{M-Pd}_2\text{Hg}_5$ aerogels with insets showing zoomed-in plots from the dashed area. f) HR-TEM image, g) high-angle annular dark-field scanning TEM (HAADF-STEM) image and corresponding energy-dispersive X-ray spectroscopy (EDXS)-based element maps of the $\text{Au-Pd}_2\text{Hg}_5$ aerogel. The inset in (f) shows the fast Fourier transform of the dashed area.

Pd₂Hg₅ aerogel. When the molar ratio of Hg–Pd is larger than 5:2 (e.g., the PdHg₃ and PdHg₅ aerogels), the ORR performance is severely suppressed, which could be ascribed to the absence of surface Pd sites (Figure S5, Supporting Information). The calculated numbers for transferred electrons in the potential range of 0–0.4 V_{RHE} gradually decreased from ≈3.8 *e*[−] for the Pd₃Hg aerogel, ≈3.3 *e*[−] for the PdHg aerogel, to ≈2.8 *e*[−] for the Pd₂Hg₅ aerogel. As the ORR kinetics gradually slow down with increasing Hg content (revealed by the Tafel slope; Figure S6, Supporting Information), the H₂O₂ selectivity shows a positive dependence on the Hg ratio (Figure 2c). As a result, the Pd₂Hg₅ aerogel shows a Tafel slope of 352.9 mV dec^{−1} and a promising H₂O₂ selectivity of 58.5% at 0.2 V_{RHE}. The improved electrocatalytic performance of the Pd₂Hg₅ aerogel can be ascribed to the isolated single-atom-like Pd sites.^[11a] Moreover, the Pd₂Hg₅ aerogel exhibits excellent stability with only 10.6% of the current density being reduced after the accelerated durability test (Figure 2d).

2.3. Design of the Heterometal-Doped M–Pd₂Hg₅ Aerogels

The electronic structure of the single-atom-like Pd sites in the Pd₂Hg₅ aerogel was further fine-tuned by isostructural substitution of heterometals while maintaining their geometric structures.^[15] Eight different metals (denoted as M, which are Au, Bi, Cu, Co, Ir, Ni, Rh, and Ru) were selected, and the resulting heterometal-doped M–Pd₂Hg₅ aerogels preserve the same morphology and backbone diameters (Figure S7, Supporting Information). Furthermore, their diffraction peaks remain unaltered compared to that of the Pd₂Hg₅ aerogel, indicative of maintained crystal structures and thus the consistent arrangement of the internal atoms (Figure 3a). The maintained geometric environment is further evidenced by the EXAFS analysis. As shown in radial distance space spectra $\chi(R)$ for the Pd K-edge (Figure 3b), the scattering path of the Pd–Hg bond is shown as the peaks at about 2.7 Å, which are identical to that of the undoped Pd₂Hg₅ aerogel. Furthermore, the EXAFS based on the Hg L₃-edge displays the same appearance before and after heterometal doping (around 2.7 Å, Figure 3c). While the geometric environment is maintained, the alterations of electronic structures have been established (Figures S8 and S9, and Table S1, Supporting Information). As shown in the Pd K-edge XANES analysis (Figure 3b), the M–Pd₂Hg₅ aerogels demonstrate similar adsorption edge positions and slightly increased white line intensities compared to that of the Pd₂Hg₅ aerogels. A similar phenomenon has been observed in the Hg L₃-edge XANES analysis (Figure 3c). This evidence suggests an electronic effect in the M–Pd₂Hg₅ aerogels based on the partial charge transfer between dissimilar atoms. Taken together, the M–Pd₂Hg₅ aerogels provide an unaltered geometric environment, which allows us to selectively investigate the electronic effects in tuning the electrocatalytic performance of the Pd sites. Taking the Au–Pd₂Hg₅ aerogel as an example, the high-resolution transmission electron microscopy (HR-TEM) reveals the same crystalline backbone with a lattice spacing of ≈0.252 nm (Figure 3f), which is consistent with the Pd₂Hg₅ aerogel. The successful doping of heterometals into the Pd₂Hg₅ aerogel was further demonstrated by the homogeneous distribution of all elements throughout the aerogel backbone (Figure 3g).

2.4. Electrocatalytic Performance of the M–Pd₂Hg₅ Aerogels

The electronic structure of the Pd sites has been fine-tuned to improve the electrocatalytic activity and selectivity. The heterometal-doped M–Pd₂Hg₅ aerogels exhibit similar CV curves compared to that of the Pd₂Hg₅ aerogel, further confirming the maintenance of the single-atom-like geometry (Figure S10a, Supporting Information). The electrocatalytic activities and selectivities were evaluated by linear sweep voltammetry (LSV) in O₂-saturated 0.1 M HClO₄ electrolyte (Figure S10b–e, Supporting Information). Table 1 summarizes the electrocatalytic performances of the M–Pd₂Hg₅ aerogels. Among them, the Au–Pd₂Hg₅ aerogel exhibits the optimal performance with a mass activity of 15.6 A g^{−1}_{noble-metal} and a H₂O₂ selectivity of 92.8% within the potential range of 0–0.4 V_{RHE} (Figure 4b). The corresponding transferred electron number is 2.1, which is close to the ideal value of 2 and suppresses most of the recently reported results (Figure 4d).^[20] Besides the H₂O₂ selectivity, the Au–Pd₂Hg₅ aerogel also exhibits excellent stability with nondegradable activity and slightly decreased selectivity (transferred electron numbers of 2.43) after the accelerated durability test (Figure 4c; Figure S11, Supporting Information). In addition, the as-designed Au–Pd₂Hg₅ aerogel shows great potential in practical H₂O₂ production in a H-cell with a production rate of 1.49 mmol g^{−1} h^{−1} and a Faradic efficiency of 71.6% (Figure S12, Supporting Information).

The correlation between electronic effects and electrocatalytic performances has been further investigated by DFT calculations. The thermodynamically favorable atomic

Table 1. Detailed comparison of the 2e ORR performances.

Electrocatalysts	H ₂ O ₂ selectivity [%]	Transferred electron numbers	References
Pd	1.2–3.5	3.9–4.0	This work
Pd ₃ Hg	6.2–14	3.7–3.9	
PdHg	26.9–41.1	3.2–3.4	
Pd ₂ Hg ₅	56.0–61.0	2.8–2.9	
PdHg ₃	9.9–15.6	3.7–3.8	
PdHg ₅	0–10.0	3.8–4.0	
Au–Pd ₂ Hg ₅	90.6–93.8	≈2.1	
Bi–Pd ₂ Hg ₅	47.3–61.0	2.8–3.0	
Co–Pd ₂ Hg ₅	67.0–80.3	2.4–2.7	
Cu–Pd ₂ Hg ₅	54.9–69.3	2.6–2.9	
Ir–Pd ₂ Hg ₅	70.3–77.0	2.5–2.6	
Ni–Pd ₂ Hg ₅	39.1–49.1	3.0–3.2	
Rh–Pd ₂ Hg ₅	23.7–36.3	3.3–3.5	
Ru–Pd ₂ Hg ₅	24.2–27.7	3.4–3.5	
PtHg/C	62.5–90	≈2.1	[6a]
PdSe NPs ^{a)}	89–91.6	≈2.1	[21]
50%PdAu	19.8–55.0	3.5–2.7	[13]
30%PdAu	50.0–60.2	2.6–2.8	[13]
PdHg/C	83–95	≈2.4	[6b]
PtAg NPs ^{a)}	67–69	≈2.6	[22]

^{a)}Note that NPs represents nanoparticles.

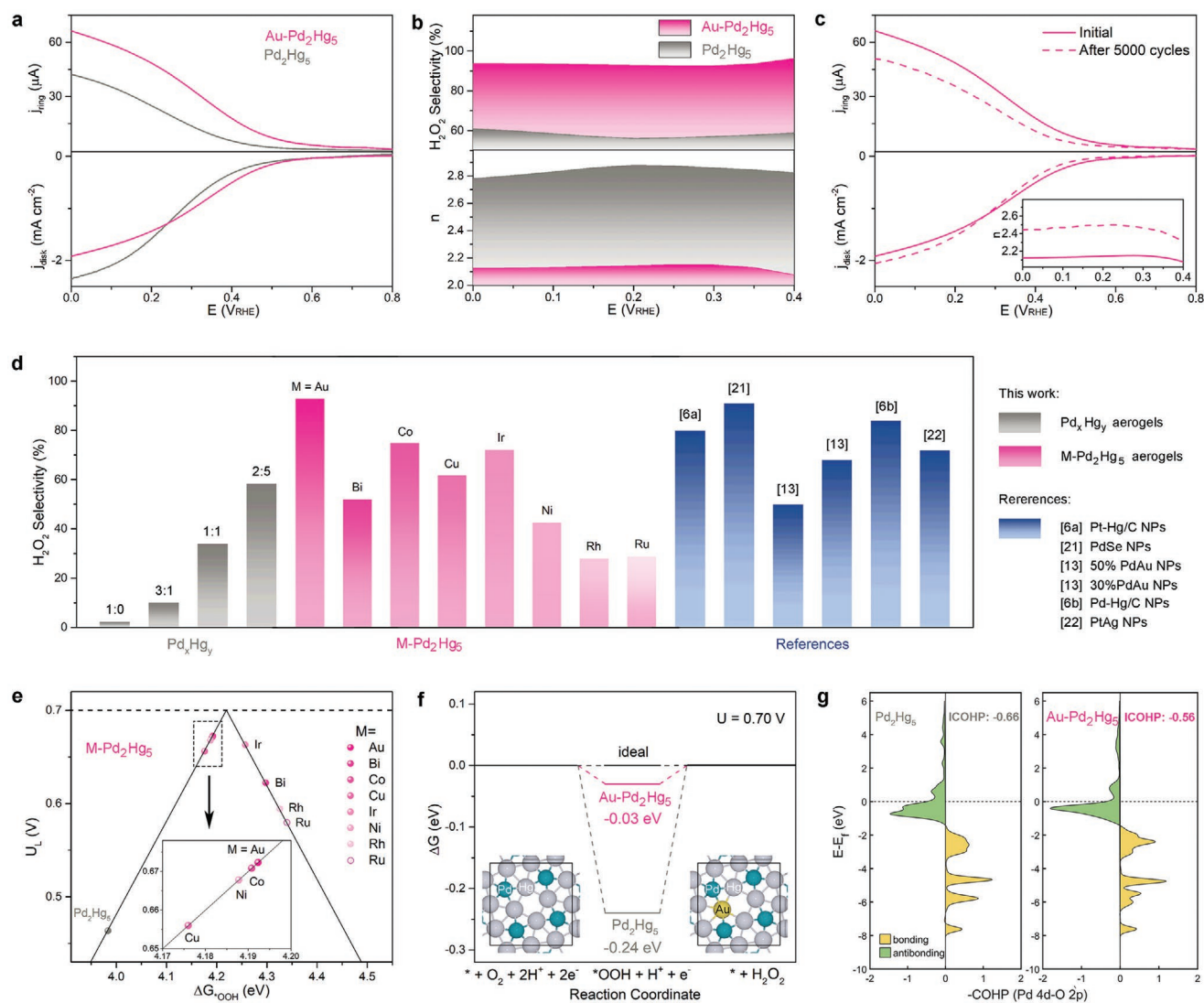


Figure 4. Optimizing the electrocatalytic performance by doping heterometals. a) LSV curves of the Pd_2Hg_5 and $\text{Au-Pd}_2\text{Hg}_5$ aerogels in 0.1 M O_2 -saturated HClO_4 at a rotation speed of 1600 rpm and a scan rate of 20 mV s^{-1} (bottom), as well as the detected H_2O_2 currents on the Pt ring electrode (top) at a fixed potential of $1.2 \text{ V}_{\text{RHE}}$. b) The corresponding H_2O_2 selectivity and transferred electron numbers. c) LSV characterization of the $\text{Au-Pd}_2\text{Hg}_5$ aerogel before and after an accelerated durability test. d) Comparison of the H_2O_2 selectivity with recently reported catalysts in acidic media. e) The calculated ORR activity volcano relationship between the limiting potential (U_L) and the free energy of $^*\text{OOH}$ ($\Delta G_{^*\text{OOH}}^*$) for the 2e pathway to H_2O_2 . The inset shows the local enlargement. f) Calculated reaction coordinate diagrams for the Pd_2Hg_5 and $\text{Au-Pd}_2\text{Hg}_5$ aerogels with insets showing the corresponding atomic configurations. This represents the 100 plane of the Pd_2Hg_5 structure. g) The crystal orbital Hamilton population (COHP) analysis of Pd–O bonding interactions of the Pd_2Hg_5 and $\text{Au-Pd}_2\text{Hg}_5$ aerogels.

configurations of the M- Pd_2Hg_5 aerogels are presented in Figure S13 (Supporting Information). In most cases, the heterometal atom occupies the Hg site to reach a thermodynamically stable condition and minimum lattice distortion. It is well known that the catalytic ORR activity can be determined by the binding strength of the key reaction intermediate $^*\text{OOH}$.^[6a,b] The calculated limiting potential (U_L) is used as an indicator of activity toward the 2e ORR, which is defined as the maximum potential at which both the 1e reduction of O_2 to $^*\text{OOH}$ and the subsequent 1e reduction of $^*\text{OOH}$ to H_2O_2 are downhill in free energy. Figure 4e shows the volcano correlation between $\Delta G_{^*\text{OOH}}^*$ and U_L for the Pd_2Hg_5 and M- Pd_2Hg_5 aerogels. The Pd_2Hg_5 aerogel positions at the left leg of the volcano plot,

indicative of a strong $^*\text{OOH}$ adsorption, which favors the dissociation of the O–O bond to drive the 4e ORR pathway. Notably, the heterometal doping dramatically lowers the adsorption strength of $^*\text{OOH}$, leading to the positioning of the M- Pd_2Hg_5 aerogels near the top of the volcano. It is worth noting that only small differences of $\Delta G_{^*\text{OOH}}^*$ were observed for Ni-, Co-, and Au-doped aerogels, which coincide with experimental data (Table 1; Figure S2, Supporting Information).

Furthermore, the optimal $\text{Au-Pd}_2\text{Hg}_5$ aerogel was elected to calculate the Gibbs free energy diagram of the 2e ORR in comparison with the undoped counterpart. As shown in Figure 4f, the $\text{Au-Pd}_2\text{Hg}_5$ aerogel presents a free energy of only -0.03 eV deviated from the ideal, which is much lower than that of the

Pd₂Hg₅ aerogel (i.e., −0.24 eV). This fact is in good agreement with the medium *OOH adsorption strength, highlighting the significance of the electronic effect by doping heterometals. The Bader charge analysis reveals that substituting Hg with Au reduces the net charge on Pd and leads to the weakened interaction between Pd 4d and O 2p orbitals, as demonstrated by the increased occupation of the antibonding states in the crystal orbital Hamilton population (COHP) analysis (Figure 4g; Figure S14, Supporting Information).

3. Conclusion

We have demonstrated a systematic strategy to optimize both geometric and electronic structures in the Pd-based pure metallic aerogels. The increasing Hg content in the Pd–Hg aerogels breaks the Pd–Pd coordination and leads to the construction of single-atom-like Pd motifs in the Pd₂Hg₅ aerogel. It also results in an increase of the selectivity toward the 2e ORR to produce H₂O₂. Using the Pd₂Hg₅ aerogel as a substrate, the electronic structure of the Pd sites was further fine-tuned by doping eight different heterometals, while maintaining their geometric environment. The introduction of heterometals leads to a controllable electronic effect in the M–Pd₂Hg₅ aerogels. Combining theoretical and experimental analyses, we reveal the role of the ligand effect in manipulating the activity and selectivity of the Pd sites and report a structure–property relationship of the M–Pd₂Hg₅ aerogels. As a result, the as-obtained Au–Pd₂Hg₅ aerogel exhibits a high H₂O₂ selectivity of 92.8% in the potential region of 0.0–0.4 V_{RHE}, which could be sustained for 10 h without decay. Our work opens a door for designing metallic aerogel electrocatalysts for H₂O₂ production and highlights the importance of electronic effects in tuning both the selectivity and activity.

Supporting Information

Supporting Information is available from the Wiley Online Library or from the author.

Acknowledgements

X.Z., C.W., and K.C. contributed equally to this work. The authors acknowledge Dr. J. Herranz for help and J. Kresse for scanning electron microscopy (SEM) measurements. Dr. D. Spittel is acknowledged for his instructions in electrochemistry. This work was funded by National Natural Science Foundation of China (Grant Nos. 52201262 and 22103047), Guangdong Basic and Applied Basic Research Foundation (Grant No. 2021A1515110920), Natural Science Foundation of Shandong Province (Grant No. ZR2022QE001), Taishan Scholars Program of Shandong Province (Program No. tsqn202211042), Swiss National Science Foundation (SNF), and German Research Foundation (DFG EY 16/18-2, EY 16/30-1, and DFG RTG 2767). C.W. acknowledges the support from the China Scholarship Council (Grant No. 202006220031). The use of the HZDR Ion Beam Center TEM facilities and the funding of TEM Talos by the German Federal Ministry of Education and Research (BMBF; 03SF0451) in the framework of HEMCP are acknowledged.

Open access funding enabled and organized by Projekt DEAL.

Conflict of Interest

The authors declare no conflict of interest.

Data Availability Statement

The data that support the findings of this study are available from the corresponding author upon reasonable request.

Keywords

electronic structure, hydrogen peroxide, metallic aerogels, oxygen reduction, single-atom catalysts

Received: December 8, 2022

Revised: February 9, 2023

Published online: March 2, 2023

- [1] a) S. C. Perry, D. Pangotra, L. Vieira, L. I. Csepei, V. Sieber, L. Wang, C. P. de Leon, F. C. Walsh, *Nat. Rev. Chem.* **2019**, *3*, 442; b) Y. Sun, L. Han, P. Strasser, *Chem. Soc. Rev.* **2020**, *49*, 6605; c) X. Shi, S. Back, T. M. Gill, S. Siahrostami, X. Zheng, *Chem* **2021**, *7*, 38.
- [2] a) X. Zhang, Y. Xia, C. Xia, H. Wang, *Trends Chem.* **2020**, *2*, 942; b) Q. Zhao, Y. Wang, W.-H. Lai, F. Xiao, Y. Lyu, C. Liao, M. Shao, *Energy Environ. Sci.* **2021**, *14*, 5444.
- [3] Y. Wen, T. Zhang, J. Wang, Z. Pan, T. Wang, H. Yamashita, X. Qian, Y. Zhao, *Angew. Chem., Int. Ed.* **2022**, *61*, e202205972.
- [4] a) Z. Y. Lu, G. X. Chen, S. Siahrostami, Z. H. Chen, K. Liu, J. Xie, L. Liao, T. Wu, D. C. Lin, Y. Y. Liu, T. F. Jaramillo, J. K. Norskov, Y. Cui, *Nat. Catal.* **2018**, *1*, 156; b) Q. Yang, W. Xu, S. Gong, G. Zheng, Z. Tian, Y. Wen, L. Peng, L. Zhang, Z. Lu, L. Chen, *Nat. Commun.* **2020**, *11*, 5478; c) Y. Xia, X. Zhao, C. Xia, Z. Y. Wu, P. Zhu, J. Y. T. Kim, X. Bai, G. Gao, Y. Hu, J. Zhong, Y. Liu, H. Wang, *Nat. Commun.* **2021**, *12*, 4225; d) Y. Bu, Y. Wang, G. F. Han, Y. Zhao, X. Ge, F. Li, Z. Zhang, Q. Zhong, J. B. Baek, *Adv. Mater.* **2021**, *33*, 2103266.
- [5] a) E. Jung, H. Shin, B. H. Lee, V. Efremov, S. Lee, H. S. Lee, J. Kim, W. Hooch Antink, S. Park, K. S. Lee, S. P. Cho, J. S. Yoo, Y. E. Sung, T. Hyeon, *Nat. Mater.* **2020**, *19*, 436; b) X. L. Zhang, X. Su, Y. R. Zheng, S. J. Hu, L. Shi, F. Y. Gao, P. P. Yang, Z. Z. Niu, Z. Z. Wu, S. Qin, R. Wu, Y. Duan, C. Gu, X. S. Zheng, J. F. Zhu, M. R. Gao, *Angew. Chem., Int. Ed.* **2021**, *60*, 26922; c) Y. Sun, L. Silvili, N. R. Sahraie, W. Ju, J. Li, A. Zitolo, S. Li, A. Bagger, L. Arnarson, X. Wang, T. Moeller, D. Bernsmeier, J. Rossmeisl, F. Jaouen, P. Strasser, *J. Am. Chem. Soc.* **2019**, *141*, 12372; d) Y. R. Zheng, S. Hu, X. L. Zhang, H. Ju, Z. Wang, P. J. Tan, R. Wu, F. Y. Gao, T. Zhuang, X. Zheng, J. Zhu, M. R. Gao, S. H. Yu, *Adv. Mater.* **2022**, *34*, 2205414.
- [6] a) S. Siahrostami, A. Verdager-Casadevall, M. Karamad, D. Deiana, P. Malacrida, B. Wickman, M. Escudero-Escribano, E. A. Paoli, R. Frydendal, T. W. Hansen, I. Chorkendorff, I. E. Stephens, J. Rossmeisl, *Nat. Mater.* **2013**, *12*, 1137; b) A. Verdager-Casadevall, D. Deiana, M. Karamad, S. Siahrostami, P. Malacrida, T. W. Hansen, J. Rossmeisl, I. Chorkendorff, I. E. Stephens, *Nano Lett.* **2014**, *14*, 1603; c) Z. Yu, S. Lv, Q. Yao, N. Fang, Y. Xu, Q. Shao, C. W. Pao, J. F. Lee, G. Li, L. Yang, X. Huang, *Adv. Mater.* **2023**, *35*, 2208101; d) S. Yang, J. Kim, Y. J. Tak, A. Soon, H. Lee, *Angew. Chem., Int. Ed.* **2016**, *55*, 2058; e) Z. Zheng, Y. H. Ng, D. W. Wang, R. Amal, *Adv. Mater.* **2016**, *28*, 9949.
- [7] J. Gao, H. B. Yang, X. Huang, S.-F. Hung, W. Cai, C. Jia, S. Miao, H. M. Chen, X. Yang, Y. Huang, T. Zhang, B. Liu, *Chem* **2020**, *6*, 658.

- [8] K. Kodama, T. Nagai, A. Kuwaki, R. Jinnouchi, Y. Morimoto, *Nat. Nanotechnol.* **2021**, 16, 140.
- [9] a) Z. W. Seh, J. Kibsgaard, C. F. Dickens, I. Chorkendorff, J. K. Nørskov, T. F. Jaramillo, *Science* **2017**, 355, eaad4998; b) J. Zhang, Y. Yuan, L. Gao, G. Zeng, M. Li, H. Huang, *Adv. Mater.* **2021**, 33, 2006494; c) L. Huang, S. Zaman, X. Tian, Z. Wang, W. Fang, B. Y. Xia, *Acc. Chem. Res.* **2021**, 54, 311.
- [10] a) X. Guo, S. Lin, J. Gu, S. Zhang, Z. Chen, S. Huang, *ACS Catal.* **2019**, 9, 11042; b) X. Yang, Y. Zeng, W. Alnough, Y. Hou, D. Higgins, G. Wu, *Adv. Mater.* **2022**, 34, 2107954; c) K. Jiang, S. Back, A. J. Akey, C. Xia, Y. Hu, W. Liang, D. Schaak, E. Stavitski, J. K. Nørskov, S. Siahrostami, H. Wang, *Nat. Commun.* **2019**, 10, 3997.
- [11] a) N. Wang, X. Zhao, R. Zhang, S. Yu, Z. H. Levell, C. Wang, S. Ma, P. Zou, L. Han, J. Qin, L. Ma, Y. Liu, H. L. Xin, *ACS Catal.* **2022**, 12, 4156; b) C. H. Choi, M. Kim, H. C. Kwon, S. J. Cho, S. Yun, H. T. Kim, K. J. Mayrhofer, H. Kim, M. Choi, *Nat. Commun.* **2016**, 7, 10922.
- [12] R. Shen, W. Chen, Q. Peng, S. Lu, L. Zheng, X. Cao, Y. Wang, W. Zhu, J. Zhang, Z. Zhuang, C. Chen, D. Wang, Y. Li, *Chem* **2019**, 5, 2099.
- [13] J. S. Jirkovsky, I. Panas, E. Ahlberg, M. Halasa, S. Romani, D. J. Schiffrin, *J. Am. Chem. Soc.* **2011**, 133, 19432.
- [14] a) B. Cai, A. Eychmüller, *Adv. Mater.* **2019**, 31, 1804881; b) N. Zion, D. A. Cullen, P. Zelenay, L. Elbaz, *Angew. Chem., Int. Ed.* **2020**, 59, 2483; c) N. Zion, J. C. Douglin, D. A. Cullen, P. Zelenay, D. R. Dekel, L. Elbaz, *Adv. Funct. Mater.* **2021**, 31, 2100963; d) X. D. Jiang, R. Du, R. Hubner, Y. Hu, A. Eychmüller, *Matter* **2021**, 4, 54.
- [15] R. Zerdoumi, O. Matselko, L. Rößner, B. Sarkar, Y. Grin, M. Armbrüster, *J. Am. Chem. Soc.* **2022**, 144, 8379.
- [16] W. Liu, A. K. Herrmann, N. C. Bigall, P. Rodriguez, D. Wen, M. Oezaslan, T. J. Schmidt, N. Gaponik, A. Eychmüller, *Acc. Chem. Res.* **2015**, 48, 154.
- [17] S. F. L. Mertens, M. Gara, A. S. Sologubenko, J. Mayer, S. Szidat, K. W. Krämer, T. Jacob, D. J. Schiffrin, T. Wandlowski, *Adv. Funct. Mater.* **2011**, 21, 3202.
- [18] M. Luo, Z. Zhao, Y. Zhang, Y. Sun, Y. Xing, F. Lv, Y. Yang, X. Zhang, S. Hwang, Y. Qin, J. Y. Ma, F. Lin, D. Su, G. Lu, S. Guo, *Nature* **2019**, 574, 81.
- [19] F. Maroun, F. Ozanam, O. M. Magnussen, R. J. Behm, *Science* **2001**, 293, 1811.
- [20] K. Jiang, J. J. Zhao, H. T. Wang, *Adv. Funct. Mater.* **2020**, 30, 2003321.
- [21] C. Yang, S. Bai, Z. Yu, Y. Feng, B. Huang, Q. Lu, T. Wu, M. Sun, T. Zhu, C. Cheng, L. Zhang, Q. Shao, X. Huang, *Nano Energy* **2021**, 89, 106480.
- [22] Y.-J. Ko, K. Choi, B. Yang, W. H. Lee, J.-Y. Kim, J.-W. Choi, K. H. Chae, J. H. Lee, Y. J. Hwang, B. K. Min, H.-S. Oh, W.-S. Lee, *J. Mater. Chem. A* **2020**, 8, 9859.